ACS OMEGA

Open Access

http://pubs.acs.org/journal/acsodf

Article

Removal of V(V) from a Mixed Solution Containing Vanadium and Chromium Using a Micropocrous Resin in a Column: Migration Regularity of the Mass Transfer Zone and Analysis of Dynamic Properties

Cui Li, EnDe You, Jia Xiang Ci, Qin Huang, Yong Sheng Zhao, Wen Zhong Li, Yu Cheng Yan, and Zhuo Zuo*

Cite This: *ACS Omega* 2024, 9, 23688−23702

Read Online

ACCESS | Metrics & More | Article Recommendations

ABSTRACT: In China, both vanadium(V) and chromium(VI) are present in wastewater resulting from vanadate precipitation (AVP wastewater) and from leaching vanadium−chromium reduction slag. Addressing environmental preservation and the comprehensive utilization of metal resources necessitates the extraction and separation of V(V) and Cr(VI) from these mixed solutions. However, their separation is complicated by very similar physicochemical properties. This study establishes a method for the dynamic selective adsorption of V(V) from such mixtures. It evaluates the impact of various operating conditions in columns on dynamic adsorption behavior. This study examines the migration patterns of the mass transfer zone (MTZ) and forecasts its effective adsorption capacity through multivariate polynomial regression and a neural network (NN) model. The NN model's outcomes are notably more precise. Its analysis reveals that C_0 is the most critical factor, with Q and H following in importance. Furthermore, the dynamic properties were analyzed using two established models, Thomas and Klinkenberg, revealing that both intraparticle and liquid film diffusion influence the rates of exchange adsorption, with intraparticle diffusion being the more significant factor. Using 3 wt % sodium hydroxide as the eluent to elute V(V)-loaded resin at a flow rate of 4 mL/min resulted in a chromium concentration of less than 3 mg/L in the V(V) eluate, indicating high vanadium−chromium separation efficiency in this method. These findings offer theoretical insights and economic analysis data that are crucial for optimizing column operation processes.

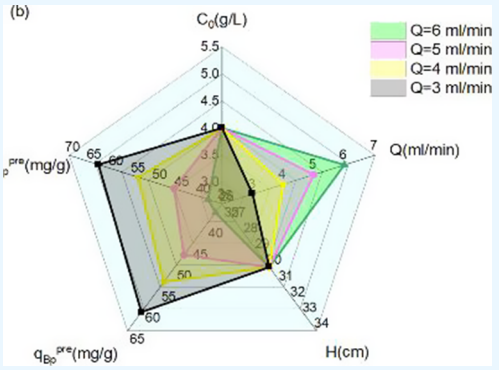

1. INTRODUCTION

The Panxi region of our country boasts abundant vanadium−chromium resources, including vanadium−titanium magnetite. Enhancing the overall recovery rate of vanadium and chromium from vanadium−titanium magnetite has significant strategic importance for improving the comprehensive utilization rate of this ore. In the current process of blast furnace smelting-converter blowing extracting vanadium using vanadium−titanium magnetite as raw material, due to the similar chemical properties of vanadium and chromium, most of the chromium in the raw materials is oxidized along with vanadium and enriched in the intermediate product—the vanadium slag—during the converter smelting process. Subsequently, chromium and vanadium are jointly leached out, forming a mixed leaching solution containing both elements.[1−3] Efficiently extracting and separating vanadium and chromium from this solution, increasing the recovery rate of both elements while also reducing environmental pollution, presents an important challenge for those working in vanadium metallurgy.

In recent years, significant advancements have been made in both domestic and international techniques for extracting vanadium from vanadium slag leachate. These include innovative leaching, column percolation, ion exchange, adsorption, high-pressure pyrolysis, and solvent extraction methods. Wen[4] introduced a novel method that uses sodium bicarbonate solution for roasting leaching of vanadium−chromium slag, achieving selective leaching and separation of vanadium from chromium. This presents a new strategy for the targeted separation of these elements. Zou[5] developed a

Received: February 13, 2024
Revised: April 8, 2024
Accepted: April 12, 2024
Published: May 22, 2024

multistep column percolation method, employing a 1.0 M oxalic acid solution to leach contaminated soil containing vanadium and chromium three times, with a solution-to-soil ratio of 0.3 mL/g. This approach resulted in 77.2% vanadium and 7.2% chromium removal rates. Xin[6] prepared a unique phosphoric acid-functionalized porous composite adsorbent, SPCCHC, combining chitosan with algae pyrolysis carbon. This adsorbent efficiently separated vanadium and chromium from mixed solutions, demonstrating high selectivity and providing an ecofriendly option for processing such mixtures. Bian[7] used a process involving ammonium chloride pressure pyrolysis, followed by acid leaching and solvent extraction, to isolate vanadium, titanium, and iron from vanadium−titanium magnetite. XRD and SEM-EDS analyses confirmed the effectiveness of this method in enhancing vanadium capture through the in situ generation of trivalent/divalent ferric chloride, facilitating the separation of vanadium and chromium. Similarly, Liu[8] utilized Aliquat 336 in solvent extraction to separate and recover vanadium and aluminum from oxalic acid-leached liquid. Luo[9] proposed the use of the ionic liquid trioctyl methylammonium chloride (TOMAC) as an extractant for an efficient and environmentally friendly recovery of V(V) from shale leaching solutions, illustrating that solvent extraction can be an effective and selective method for separating vanadium and chromium.

The ion exchange method[10,11] stands out among various techniques due to its advantages, such as recyclability, efficient vanadium and chromium separation, and cost-effectiveness. In this research, a column exchange technique has been developed, capitalizing on the different behaviors of vanadium and chromium in solution to selectively adsorb V(V) from a mixed solution. The effective adsorption capacity was obtained using both multivariate polynomial regression and neural network (NN) models. Furthermore, the dynamic properties were analyzed using two established models, Thomas and Klinkenberg, revealing that both intraparticle and liquid film diffusion influence the rates of exchange adsorption, with intraparticle diffusion being the more significant factor. This research offers both technical and theoretical guidance for enhancing the overall recovery of vanadium and chromium from wastewater produced during vanadium precipitation as well as from the leachate of reduced vanadium−chromium slag.

2. EXPERIMENTAL MATERIALS AND METHODS

2.1. Experimental Materials. Column experiments were carried out in glass columns equipped with a Dex-V resin. These columns measured 40 cm in height and had an internal diameter of 1.5 cm. We employed a macroporous anionic exchange resin, Dex-V, as the adsorbent. All of the chemicals utilized in our experiments were of analytical grade. For the process of resin transformation and regeneration, we used 0.85 M HCl to regenerate the resin and 0.5 M NaOH served as the eluent for extracting vanadium. The pH levels of solutions were adjusted using 0.1 M NaOH and 0.1 M H_2SO_4. In order to alter the valence states of vanadium and chromium, $NaHSO_3$ and H_2O_2 were used as a reductant and a mild oxidant, respectively. Stock solutions containing 10 g/L V(V) and 4 g/L Cr(VI) were prepared by dissolving Na_3VO_4 and Na_2CrO_4, respectively.

2.2. Selectively Reducing Cr(VI). To selectively adsorb vanadium, V(V) and Cr(VI) were first reduced to V(IV) and Cr(III) by the reductant, respectively. Subsequently, V(IV) was selectively oxidized to V(V) by a weak oxidant, resulting in the formation of V(V) anionic groups, while Cr(III) remained in its trivalent cationic form.[1] Subsequently, the pH of the leachate was adjusted to 3.0.

2.3. Experimental Method and Principle. The study commenced with a diluted mixture of V(V) and Cr(VI) stock solutions, utilized as the feed for the column, to investigate the optimal operating conditions for ion exchange processes. It aimed to predict the adsorption capacity of the column and optimize its conditions using nonlinear programming techniques. Following this, the resin-treated eluent with 0.5 M NaOH underwent several stages, including precipitation, purification, and roasting, to produce V_2O_5. The solution, after vanadium removal, undergoes sequential washing, precipitation, and roasting to produce Cr_2O_3. The process flow for the separation of vanadium and chromium is shown in Figure 1.

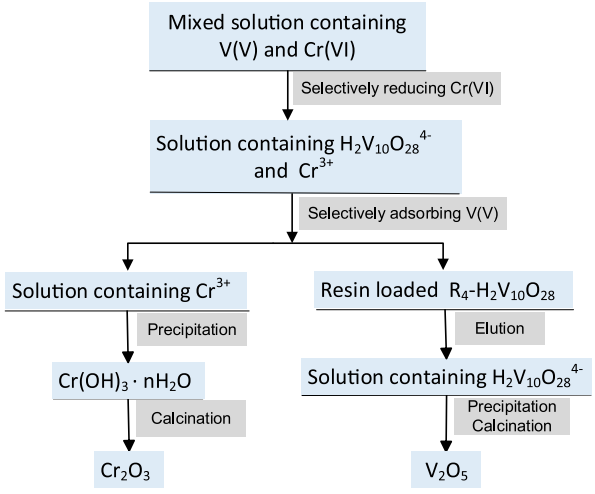

Figure 1. Process flow for the separation of vanadium and chromium.

V(V), pretreated through redox reactions in the leachate, was selectively absorbed by the resin as $H_2V_{10}O_{28}^{4-}$,[1,12] while Cr^{3+} remained unabsorbed in the solution. The active ion in the Dex-V resin is Cl^-. During adsorption, $H_2V_{10}O_{28}^{4-}$ ions move through the resin particle's surface liquid film layer by mass transfer, then diffuse into the macropores to exchange with the mobile Cl^- ions on the reactive sites. The replaced Cl^- ions exit the resin particles, moving through the liquid film layer back into the solution. The absorption process of V(V) by Dex-V resin can be described as follows:[1]

$$H_2V_{10}O_{28}^{4-}{}_{(l)} + \overline{4R - Cl_{(s)}} \rightarrow \overline{R_4 - H_2V_{10}O_{28(s)}} + 4Cl^-{}_{(l)}\ (pH = 3.0) \quad (1)$$

2.4. Column Experiments. A mixed solution of V(V) and Cr(III) was prepared using stock solutions of V(V) and Cr(VI). We created mixtures with varying concentrations of V(V) (2, 4, 6, and 10 g/L) and a constant concentration of Cr(VI) at 2.4 g/L for the feed solutions. These solutions were then passed through a column packed with resin at various bed heights (25, 30, and 35 cm) using a peristaltic pump set to different flow rates (3, 4, 5, and 6 mL/min). Samples were continuously collected from the column outlet at regular

https://doi.org/10.1021/acsomega.4c01417
ACS Omega 2024, 9, 23688−23702

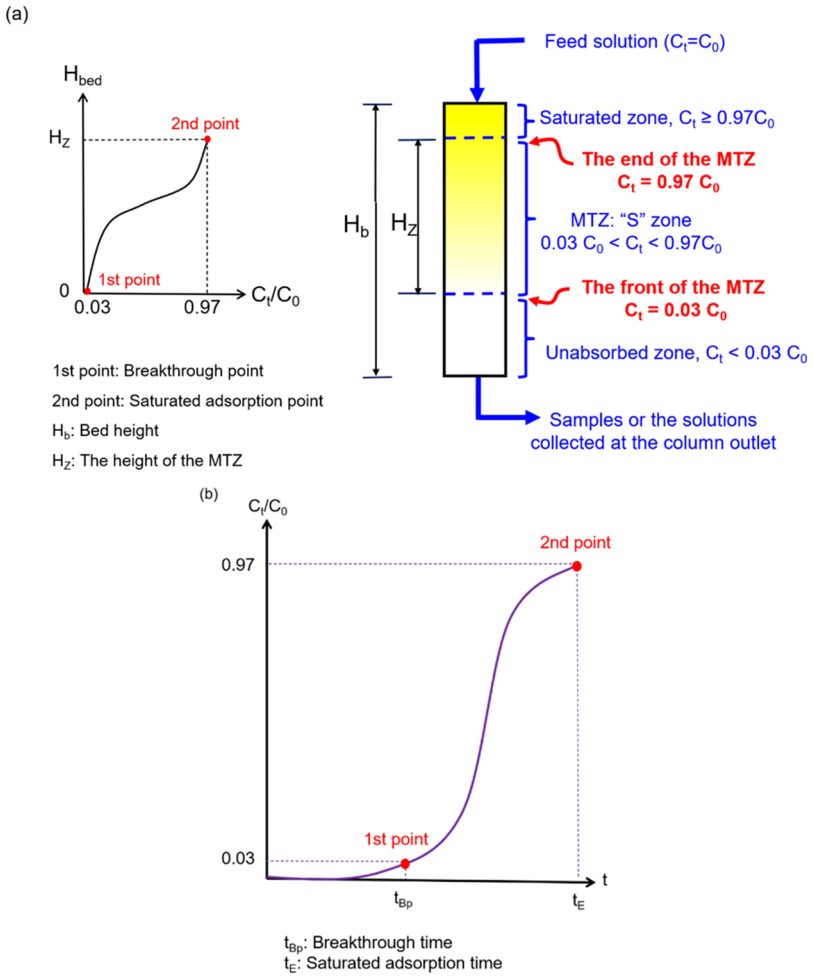

Figure 2. (a) Description of the MTZ; (b) Variation in V(V) concentration in the solution collected at the column outlet over time.

intervals and analyzed using inductively coupled plasma-atomic emission spectrometry (Optima 4300 DV, PerkinElmer, USA). The elution of vanadium-loaded resin occurred when the V(V) concentration at the column outlet reached 97% of its initial value using 0.5 M NaOH at a flow rate of 4 mL/min to obtain the eluent. This data helped predict the optimum operating conditions for the column.

During the adsorption process, breakthrough curves[13,14] (BTCs) were generated, defining the breakthrough time (t_{Bp}) when V(V) concentration at the outlet was 3% of the feed concentration and the saturated adsorption time (t_E) when it reached 97%.

2.5. Analysis of the Column Data. As the feed solution flows through the column, vanadium anionic groups move from the solution into the resin's active sites, replacing chloride ions (Cl-). The mass transfer zone (MTZ) gradually moved downward through the bed. Once the MTZ front reaches the bed's bottom, vanadium(V) starts to be detected in the outlet samples, with its concentration increasing over time. A breakthrough is identified when the concentration of vanadium(V) in these samples hits 3% of its concentration in the feed solution. The methodologies proposed by Michaels[15] and Lukchis[16] are suitable for examining how varying column operating conditions affect breakthrough behavior and for investigating MTZ's migration patterns.

2.5.1. Effective Utilization Rate of the Column. The utilization rate of the column, denoted as η, is essentially the ratio of V(V) adsorption at the breakpoint (A_{Bp} in mg) to its total adsorption at equilibrium (A_E in mg). The fraction of adsorption capacity, F, is the ratio of the V(V) amount adsorbed per unit height of the MTZ, A_Z (mg), to the total V(V) quantity passing through the MTZ, A_{max} (mg). Theoretically, η is directly related to F, as demonstrated by the equations below:

$$A_{Bp} = \int_0^{V_{Bp}} (C_0 - C_V)dV = Q^* \int_0^{t_{Bp}} (C_0 - C_t)dt \quad (2)$$

$$A_Z = \int_{V_{Bp}}^{V_E} (C_0 - C_V)dV = Q^* \int_{t_{Bp}}^{t_E} (C_0 - C_t)dt \quad (3)$$

$$A_{max} = C_0(V_E - V_{Bp}) = C_0(t_E - t_{Bp}) \times Q \quad (4)$$

$$\eta = \frac{A_{Bp}}{A_E} = \frac{Q^* \int_0^{t_{Bp}} (C_0 - C_t)dt}{Q^* \int_0^{t_E} (C_0 - C_t)dt} = \frac{\int_0^{t_{Bp}} (C_0 - C_t)dt}{\int_0^{t_E} (C_0 - C_t)dt} \quad (5)$$

$$F = \frac{A_Z}{A_{max}} = \frac{Q^* \int_{t_{Bp}}^{t_E} (C_0 - C_t)dt}{C_0(t_E - t_{Bp})^*Q} = \frac{\int_{t_{Bp}}^{t_E} (C_0 - C_t)dt}{C_0(t_E - t_{Bp})} \quad (6)$$

https://doi.org/10.1021/acsomega.4c01417
ACS Omega 2024, 9, 23688−23702

$$\eta = \frac{\int_0^{t_{Bp}} (C_0 - C_t)dt}{\int_0^{t_E} (C_0 - C_t)dt} = 1 - \frac{\int_{t_{Bp}}^{t_E} (C_0 - C_t)dt}{\int_0^{t_E} (C_0 - C_t)dt} = 1 - \frac{\int_{t_{Bp}}^{t_E} (C_0 - C_t)dt}{\int_0^{t_{Bp}} (C_0 - C_t)dt + \int_{t_{Bp}}^{t_E} (C_0 - C_t)dt} \quad (7)$$

$$\eta \approx 1 - \frac{FC_0(t_E - t_{Bp})}{C_0 t_{Bp} + FC_0(t_E - t_{Bp})} \quad (8)$$

where t_{Bp} is the breakpoint and t_E is the equilibrium point. A_{Bp} and A_E are the V(V) adsorption amount of the column at t_{Bp} and t_E, respectively. V_{Bp} and V_E are the volume of the solution flowing through the column at $t_{Bp}$and t_E, respectively.

2.5.2. Height and Migration Rate Analysis of the MTZ. The MTZ[17] typically denotes the area where ion exchange reactions occur between the zone of saturation and the unsaturated region. The MTZ's height indicates the efficiency of vanadium(V) adsorption by the resin in the column. A quicker adsorption process results in a shorter MTZ height,[18] indicating lower mass transfer resistance. Conversely, a taller MTZ suggests a slower adsorption rate and higher resistance in the mass transfer process.[19]

In an adsorption column, the MTZ typically forms an S-shaped curve along the column axis. The curve flattens at both ends, suggesting that the MTZ is expanding and extending its length. This extension leads to a decreased mass transfer driving force, due to the reduced concentration gradient at the MTZ's front. Furthermore, the resin's limited adsorption capacity slows down the rate at which it can adsorb V(V), as part of the resin has already absorbed some V(V) anionic groups. However, in the MTZ's central area, where the resin first encounters high concentrations of V(V) anionic groups, it shows strong adsorption capacity. This causes the MTZ curve to contract. As the adsorption progresses, the MTZ moves downward along the column. The MTZ's end, marking the saturation zone's bottom, and its front difference define the MTZ's height, denoted as H_z, illustrated in Figure 2.

t_{Bp} is defined as the moment when the MTZ front reaches the column's end, initiating breakthrough behavior. Similarly, t_E marks the time when the MTZ's end aligns with the column's end, resulting in resin saturation within the column. From this analysis, it is evident that the time (t_Z) needed for the MTZ to traverse a distance equivalent to its height (H_Z) equals the difference between t_E and t_{Bp}. Consequently, the MTZ's migration rate (U_Z) can be described by eq 10:

$$t_Z = t_E - t_{Bp} \quad (9)$$

$$U_Z = H_Z/t_Z \quad (10)$$

When the MTZ descends from the bed's top to its tail, it travels a distance equal to the column's bed height (H_b). The duration (t) of this process equals the difference between t_E and the MTZ's initial formation time (t_f), as demonstrated in eq 11. Furthermore, the MTZ's migration rate (U_Z) is defined in eq 12:

$$t = t_E - t_f \quad (11)$$

$$U_Z = H_b/t \quad (12)$$

Based on the equations from 9 to 12, eq 13 can be obtained as follows:

$$H_Z/(t_E - t_{Bp}) = H_b/(t_E - t_f) \quad (13)$$

According to eq 6, we can assess the adsorption capacity for each unit of MTZ height using parameter F. When $F = 1$, it suggests that the resin within the column is nearly saturated at t_{Bp}, resulting in an exceptionally small MTZ height per unit. This scenario also leads to a prolonged period before the MTZ front reaches the column's bottom, implying the MTZ forms very quickly—practically in no time (t_f is almost 0). Conversely, when $F = 0$, it indicates a low adsorption capacity per unit of MTZ height, stretching the MTZ length considerably and causing the MTZ front to reach the bottom of the column rapidly. This condition is expected to significantly extend the MTZ's formation time (t_f is roughly equal to t_Z). Thus, the equation below represents the correlation between t_Z of the MTZ and parameter F:

$$t_f = (1 - F)t_Z = (1 - F)(t_E - t_{Bp}) \quad (14)$$

By combining eqs 13 and 14, the height of the MTZ can be obtained as

$$H_Z = \frac{H_b(t_E - t_{Bp})}{t_{Bp} + F(t_E - t_{Bp})} \quad (15)$$

where $H_Z$is the height of the MTZ itself, H_b is the bed height of the column, t_f is the formation time of the MTZ, and t_E is the time required for the resin within the column to reach saturation adsorption.

2.5.3. NN Model. An NN model[20−22] was developed to predict the removal efficiency of V(V) in column exchange experiments. The design of the NN model includes several key components: the input layer, hidden layer, output layer, connection weights and biases, activation functions, and summing nodes. Mean square errors (MSE) serve as the loss function, Prelu is used as the activation function, and stochastic gradient descent (SGD) is the method for gradient descent. Computations were carried out using Pycharm software. The maximum number of epochs for training cycles was set to 2000. The magnitude of the loss, which is used to assess performance, is defined by eq 16:

$$\mathrm{MSE} = \frac{1}{n}\sum_{i=1}^{n} (y_i - \hat{y}_i)^2 \quad (16)$$

2.5.4. Models for Dynamic Properties. 2.5.4.1. Thomas Model. The Thomas model[22] suggests that ion exchange in the column operates like piston flow, with isothermal adsorption following the Langmuir isotherm equation. Intraparticle diffusion mass transfer is the sole rate-limiting factor, disregarding liquid phase backmixing effects. The relationship is derived as follows:

$$\ln\left(\frac{C_o}{C_t} - 1\right) = \frac{k_T q_o m}{Q} - k_T C_o t \quad (17)$$

where k_T (L/min·g) is the rate constant of the Thomas model, q_o (mg/g) is the theoretical maximum adsorption capacity of the resin, m (mg) is the mass of the numerals, and t (min) is the adsorption time.

https://doi.org/10.1021/acsomega.4c01417
ACS Omega 2024, 9, 23688−23702

2.5.4.2. Klinkenberg Model. Assuming that the mass transfer driving force is linearly related to the concentration gradient of the liquid phase, and ignoring the effects of axial backmixing, the following expression can be derived according to Klinkenberg:[23−25]

$$\frac{C}{C_t} \approx \frac{1}{2}\left[1 + \mathrm{erf}\left(\sqrt{\tau} - \sqrt{\xi} + \frac{1}{8\sqrt{\tau}} + \frac{1}{8\sqrt{\xi}}\right)\right] \quad (18)$$

$$\xi = (k_g k_d z/u)((1-\varepsilon)\varepsilon) \quad (19)$$

$$\tau = k_g(t - (Z/u)) \quad (20)$$

where ξ is the dimensionless length transformation coordinate, and τ is the dimensionless time transformation coordinate. $k_g$is the overall diffusion coefficient, and $k_f$is the external fluid film mass transfer coefficient. $D_p$is the pore diffusion coefficient within the particle. According to Henley,[25] the following expression can be derived from the equation for the overall diffusion coefficient provided:

$$\frac{1}{k_g k_d} = \frac{R_p}{3k_f} + \frac{{R_p}^2}{15D_p} \quad (21)$$

$$\mathrm{Sh} = 1.09\varepsilon^{-2/3}\mathrm{Re}^{1/3}Sc^{1/3} \quad (22)$$

$$Sh = \frac{2k_f R_p}{D_m} \quad (23)$$

The Sherwood number, denoted as *Sh*, quantifies the ratio of the resistance to diffusion at the fluid boundary compared to the overall mass transfer resistance. The Schmidt number, *Sc*, measures the ratio of momentum transfer to mass transfer, indicating how these two processes compare in fluid flow. The Reynolds number, *Re*, represents the ratio of inertial forces to viscous forces, which is a crucial factor in determining the flow characteristics of fluids. D_m, with units of m^2/s, is the diffusion coefficient for the adsorbed material in the water-soluble phase. The density of the liquid phase is represented by ρ in kg/m^3, and R_p, expressed in meters (m), is the radius of the resin particle. These parameters are essential for understanding and modeling the behavior of particles and fluids in various engineering and scientific applications.

3. RESULTS AND DISCUSSION

3.1. Effect of Column Operating Conditions on V(V) Adsorption in Column. *3.1.1. Effect of Flow Rate.* At a pH of 3.0, a mixed solution with a concentration of 4 g/L V(V) and 2.4 g/L Cr(VI) was passed through a column with a bed height of 30 cm at flow rates of 3, 4, 5, and 6 mL/min. Figure 3 displays the effects of different flow rates on the BTCs of the dynamic adsorption of V(V).

Increasing the feed solution flow rate from 3 to 6 mL/min reduced the empty bed contact time[26−28] (EBCT) from 10.4 to 5.2 min. Simultaneously, the Dex-V resin's adsorption capacity for vanadium decreased from 168 to 115 mg/g. As shown in Figure 3, a higher flow rate speeds up both bed penetration and saturation velocities, leading to quicker breakthrough times, smaller penetration and saturation volumes, and a reduced saturation adsorption volume.

Figure 3 illustrates a distinct feature of the BTCs for vanadium(V) exchange. As the feed solution's flow rate increases, the curve's shape noticeably shifts away from the classic S-shape. More precisely, the curve's lower portion morphs from being concave to convex. This change likely results from the heightened mass transfer driving force, prompted by the increased flow rate, which accelerates the mobility of V(V) anions in the solution. Consequently, the feed solution spends less time in the exchange column, enabling V(V) anions to move through the column faster and exit with the effluent. This rapid transit reduces the chances for V(V) anions to interact with the resin's active sites and participate in exchange reactions. The outcome is a shorter MTZ and a more noticeable upward bulge in the penetration curve, a trend that becomes especially evident at lower exchange capacities.

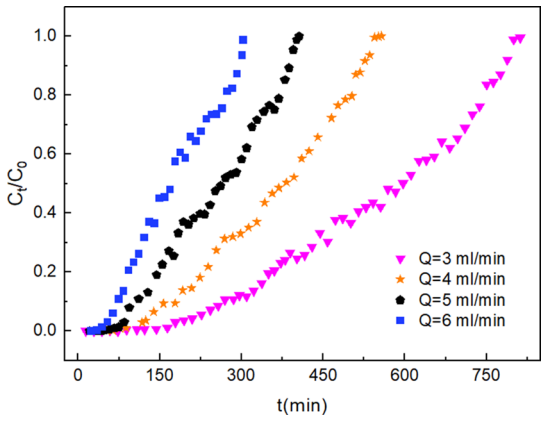

Figure 3. BTCs of V(V) adsorption at different flow rates.

Figure 3 demonstrates that the BTCs exhibit a smoother trend at lower flow rates, suggesting that the resin has a higher adsorption capacity. In contrast, a sharper change in the BTCs signifies a quicker reach to breakthrough and saturation, indicating a decreased adsorption capacity of the resin. These findings align with research conducted by Ma[29] and Schaefer.[30] Choosing an appropriate flow rate requires balancing several factors to meet the processing demands and achieve optimal adsorption efficiency. At flow rates of 3, 4, 5, and 6 mL/min, the resin's saturated adsorption capacities were recorded at 168, 148, 138, and 115 mg/g, respectively, with corresponding saturation times of 613, 557, 507, and 455 min. Below 4 mL/min, a minor increase in flow rate gradually reduces the adsorption capacity while significantly decreasing the adsorption time. Above 4 mL/min, the trend reverses. Thus, a flow rate of 4 mL/min was chosen for further experiments with V(V) solution, considering the balance between adsorption capacity and time.

3.1.2. Effect of Bed Height. At a pH of 3.0, a mixed solution with 4 g/L V(V) and 2.4 g/L Cr(VI) was passed through columns of different bed heights (25, 30, and 35 cm) at a constant feed rate of 4 mL/min. The effects of these varying bed heights on the BTCs for the dynamic adsorption of V(V) are illustrated in Figure 4.

According to Figure 4, the BTCs become more S-shaped and their transitions from start to end are smoother with increasing bed height. This also results in higher breakthroughs and total outflow volumes. This effect is due to the larger amount of Dex-V resin in taller beds, offering more effective adsorption sites for V(V). Additionally, a taller bed extends the contact time between the resin and solution phases, leading to lower V(V) concentrations at the column's output. As a result, both the breakthrough and saturation times are extended.

https://doi.org/10.1021/acsomega.4c01417
ACS Omega 2024, 9, 23688−23702

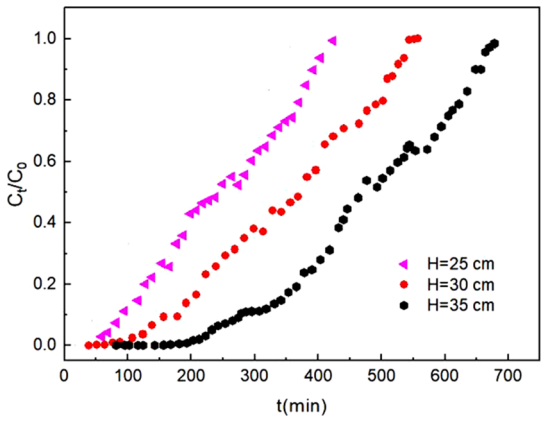

Figure 4. BTCs of V(V) adsorption at different bed heights.

Furthermore, a greater bed height improves mass transfer and enlarges the contact area between V(V) anions and the resin's active adsorption sites, enhancing the column's dynamic adsorption capacity.[31,32] However, an excessively tall bed height increases the resistance, raising both operational costs and time. Therefore, after evaluating these aspects, a bed height of 30 cm was selected for subsequent experiments.

3.1.3. Effect of Initial V(V) Concentration. At a pH of 3.0, a solution containing 2.4 g/L Cr(VI) and varying concentrations of V(V) at 2, 4, 6, and 10 g/L was passed through a column with a bed height of 30 cm and a flow rate of 4 mL/min. The BTCs for V(V) adsorption at these different concentrations are presented in Figure 5.

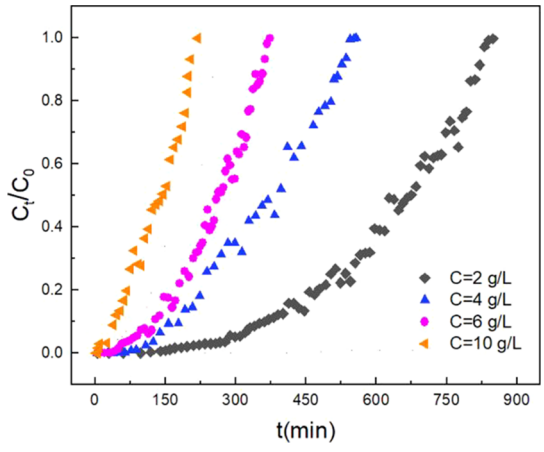

Figure 5. BTCs of V(V) adsorption at different V(V) concentrations.

In the adsorption process, at the 200th minute, the ratio of C_t/C_0 was observed to be 0.02, 0.18, 0.28, and 0.98 for initial V(V) concentrations of 2, 4, 6, and 10 g/L, respectively. However, when the initial concentration of V(V) in the feed solution is excessively high, there is not sufficient time for the V(V) anionic groups to diffuse and interact with the resin's adsorption sites as the MTZ moves downward through the column. This results in inadequate interaction with active sites and diminishes the column's effective utilization rate.

Figure 5 demonstrates that as the initial concentration of V(V) increases, the BTCs become steeper, indicating that the adsorption process reaches saturation more quickly. Furthermore, higher initial concentrations of V(V) result in smaller breakthrough and saturation volumes. This is due to the larger concentration gradient of V(V) inside and outside the resin particle, which enhances the mass transfer driving force for the anionic groups of V(V),[33,34] thereby improving the efficiency of diffusion mass transfer. Additionally, a higher concentration of the V(V) feed solution shortens the length of the MTZ,[35,36] suggesting that the V(V) concentration affects the breakthrough and saturation times by altering the rates of mass transfer and diffusion efficiency.

A higher concentration of the V(V) feed enhances the availability of active adsorption sites for reacting with V(V) anionic groups, leading to quicker adsorption. This results in earlier breakthrough and saturation times. Moreover, under identical conditions, the resin's adsorption capacity increases with the concentration of V(V). Specifically, the Dex-V resin reached its maximum adsorption capacity for V(V) at 176 mg/g with a bed height of 30 cm. This capacity is notably greater than the best achieved in static adsorption processes (133 mg/g), obtained at a starting V(V) concentration of 10 g/L and a flow rate of 4 mL/min. These outcomes align with findings by Chow[37] and Al-Jaser,[38] who also reported similar trends in BTCs with varying initial concentrations of V(V).

3.2. Migration Regularity of the MTZ and the Optimization of V(V) Dynamic Adsorption Conditions. *3.2.1. Effective Utilization Rate of the Column under Different Column Operating Conditions.* The shape of BTCs indicates that a higher F value signifies a stronger adsorption capacity of the resin over time. This implies a greater adsorption capacity per unit MTZ height, leading to a smoother BTC trend from the beginning t_{Bp} to the end t_E. Theoretically, both increasing bed height and reducing flow rate enhance column operating conditions, boosting vanadium(V) adsorption capacity throughout the process. Consequently, the resin's V adsorption amount increases from t_{Bp} to t_E, indicating a rise in adsorption capacity and column efficiency per unit MTZ height. Table 1 presents the actual F

Table 1. Characteristic Parameters of the MTZ

C_0 g/L	Q mL/min	H cm	t_f min	t_Z min	F	A_Z g	A_{max} g	H_Z cm	U_Z cm/min	N_Z	q_{Ep}^{exp} mg/g	q_{Bp}^{exp} mg/g	η%
2	4	30	228	615	0.63	3.10	4.92	30	0.05	1.01	148	53.7	28
6	4	30	132	314	0.58	4.37	7.53	39	0.12	0.77	168	40.7	16
10	4	30	63	209	0.70	5.84	8.34	40	0.19	0.75	176	11.7	5
4	3	30	302	635	0.52	3.99	7.62	37	0.06	0.80	161	60.6	22
4	5	30	161	323	0.50	3.25	6.47	40	0.12	0.76	138	47.1	20
4	6	30	134	250	0.47	2.78	5.99	44	0.18	0.68	115	37.1	18
4	4	25	194	359	0.46	2.63	5.74	40	0.11	0.63	121	32.9	14
4	4	30	216	440	0.51	3.60	7.04	39	0.09	0.78	158	53.5	21
4	4	35	186	455	0.59	4.31	7.28	32	0.07	1.08	190	87.6	33

https://doi.org/10.1021/acsomega.4c01417
ACS Omega 2024, 9, 23688−23702

values under various operating conditions, confirming the theoretical predictions.

Table 1 illustrates the relationship between the column effectiveness and operating conditions. Increasing bed height, decreasing feed rate, and lowering initial V(V) concentrations improve column utilization. However, very slow feed rates increase back mixing, and higher bed heights yield more resistance, raising costs and extending operation times. Thus, a comprehensive consideration of factors is crucial in experiments.

The MTZ's considerable height necessitates a theoretical bed height significantly larger than the actual MTZ length. Yet, the actual bed height is reduced below the theoretical requirement due to heightened bed resistance from increasing bed height. Consequently, the effective utilization rate remains modest, peaking at 33% under specific experimental conditions—achieved with a flow rate of 4 mL/min, a bed height of 35 cm, and an initial V(V) concentration of 4g/L.

3.2.2. Migration Regularity of the MTZ. Figure 6 illustrates the correlation between the MTZ height and column operating conditions. The MTZ height diminishes as the bed height increases, but it elevates with higher initial V(V) concentration and greater solution flow rates. An increase in flow rate necessitates a larger MTZ to compensate for V(V)'s reduced residence time, thereby raising the MTZ's height. Conversely, a higher initial V(V) concentration leads to an increase in the MTZ height to accommodate more V(V) ions through additional active adsorption sites. Moreover, increasing the bed height enhances the column's adsorption efficacy by offering ample adsorption sites for V(V), which in turn reduces the MTZ height.

Figure 2 illustrates the MTZ as the area between the two dotted lines. The top dotted line indicates the boundary where C/C_0 = 0.97, marking everything above this line as the saturated adsorption zone. Conversely, the bottom dotted line marks the boundary, where C/C_0 equals 0.03. The MTZ's migration rate mirrors the downward expansion of the saturated adsorption zone. From eq 13, we have derived formulas for both the MTZ's migration rate (eq 24) and its migration distance (eq 25):

$$U_t = H_t/(t - t_f) = H_b/(t_E - t_f) \quad (24)$$

$$H_t = H_b(t - t_f)/(t_E - t_f) \quad (25)$$

Figure 7 illustrates the correlation between C_t/C_0 and the migration distance of the MTZ during the experiments. With a constant flow rate of 4 mL/min, once the column resin became saturated (C_t/C_0 = 0.97), the MTZ heights for columns with bed heights of 25, 30, and 35 cm were recorded as 40, 39, and 32 cm, respectively. Furthermore, the respective migration distances of the MTZ at saturation were measured at 24.50, 28.75, and 34.75 cm.

The experimental results show that as the value of C_t/C_0 approaches 0.97, the migration distance of the MTZ changes, depending on the bed height; it increases with the bed height. Theoretically, the MTZ's front moves downward toward the bottom of the column. However, if the height of the nonreactive region, which does not undergo any exchange reaction, is less than the MTZ's height, it fails to accommodate a complete MTZ. As a result, the concentration of V(V) at the column outlet reaches and then surpasses the breakthrough value (C_t/C_0 = 0.03), eventually reaching the saturation level. The longer the MTZ within the column, the less efficiently it is utilized, leading to a shorter MTZ migration distance. Consequently, this results in a quicker reach of both the breakthrough and saturation values for the concentration of V(V) at the column outlet. These findings are consistent with theoretical predictions.

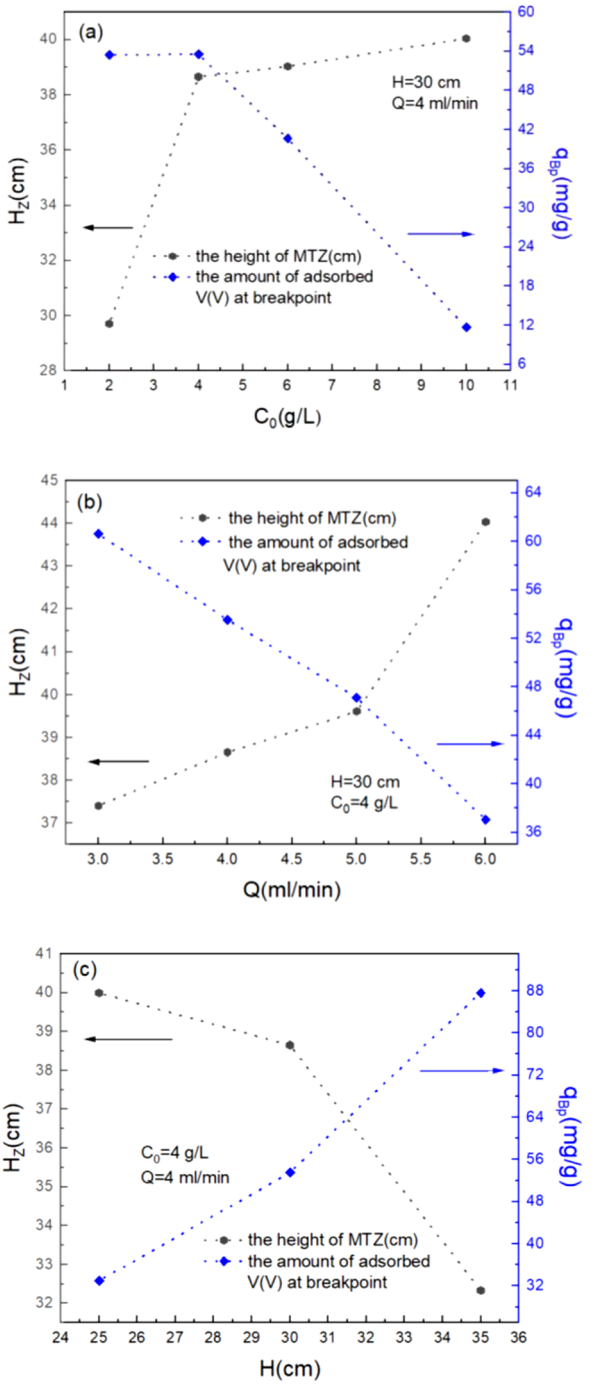

Figure 6. Trends of the MTZ height and the effective adsorption capacity with (a) initial V(V) concentration, (b) flow rate of feed solution, and (c) bed height.

The column's efficiency can also be measured by a parameter known as N_Z, besides η. N_Z represents the number of MTUs calculated as the ratio of the bed height to the height of the MTZ. According to eq 26,[39−41] N_Z indirectly indicates the rate at which resin adsorbs V(V):

https://doi.org/10.1021/acsomega.4c01417
ACS Omega 2024, 9, 23688−23702

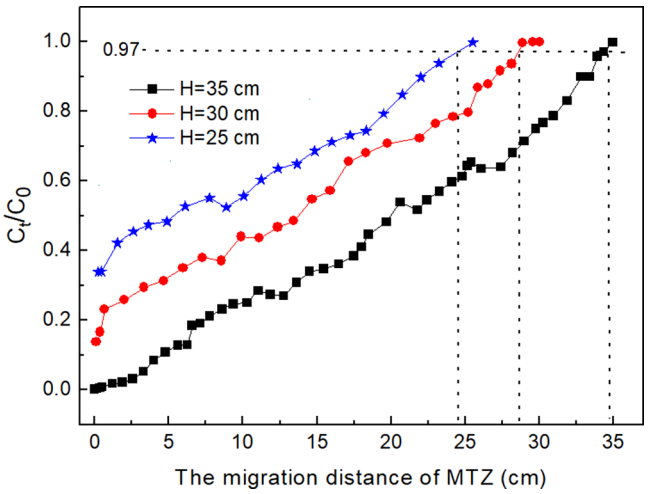

Figure 7. Relationship between C_t/C_0 and the migration distance of the MTZ.

$$N_Z = \frac{H_b}{H_Z} = = \frac{t_{Bp} + F(t_E - t_{Bp})}{(t_E - t_{Bp})} \quad (26)$$

The concentration change of V(V) in the solution over a specific period is denoted by $C_1 - C_2$. The mass transfer driving force, expressed as $C^* - q^*$, depends on the average concentration difference of V(V) between the solution and the resin phases. N_z is then defined as the ratio of $C_1 - C_2$ to $C^* - q^*$, as detailed in eq 27. Greater N_z values signify a larger concentration gradient of the adsorbate per unit of mass transfer driving force, indicating V(V)'s faster migration from the liquid to the solid phase during adsorption. Therefore, a higher N_z value reflects an increased adsorption efficiency of the resin:

$$N_Z = \frac{C_1 - C_2}{C^* - q^*} \quad (27)$$

Table 1 demonstrates that the number of mass transfer units (MTUs) decreases with rising flow rates and initial V(V) concentrations but increases when the bed height is raised. The higher flow rate amplifies spatial potential resistance, accelerating the movement of the MTZ and hastening the breakthrough and saturation points. Consequently, the residual concentration of V(V) in the resin's interstitial spaces grows, reducing the solute's concentration gradient and thus the number of MTUs. Conversely, at a constant flow rate but with higher initial V(V) concentrations, more resin is needed to adsorb the additional V(V), enlarging the MTZ and decreasing MTUs, which diminishes the column's efficiency.

Increasing the bed height extends the migration distance of the MTZ, enhancing the interaction between the resin and V(V). This results in a higher distribution ratio of V(V) across the solid−liquid phase. Consequently, at the adsorption end point, less V(V) remains in the column's solution. Essentially, a greater number of MTUs correlates to a higher saturated adsorption capacity of the resin and improves the efficiency of the exchange column.

3.2.3. Prediction of Effective Adsorption Capacity of the Column. The effective adsorption capacity of the resin, q_{Bp}, is defined as its capacity at breakthrough. It is calculated with the equation $q_{Bp} = A_{Bp}/m$, where A_{Bp} represents the volume (V) of adsorbate at breakthrough and m is the resin's mass.

Table 2 shows the resin's effective adsorption capacity (q_{Bp}^{exp}) under different column operating conditions, including bed heights, initial V(V) solution concentrations, and flow rates. The predicted values ($q_{Bp}^{pre\_MPR}$) were calculated using multivariate polynomial regression, as outlined in eq 28:

$$q_{Bp} = 129.0 - \left(8.3C + \frac{89.5}{C^2}\right) - \left(6.8Q - \frac{27.6}{Q}\right) + \left(2.2H^{1.5} - 12.5H\right) \quad (28)$$

where H, C, and Q represent the bed height, initial V(V) concentration in the solution, and flow rate of the feed solution passing through the column, respectively.

Figure 8 displays a comparison between the experimental and predicted adsorption capacities, revealing that the predicted values closely match the experimental ones. The correlation coefficient R^2 for the fit is 0.993, with a standard error of 2.53. The significance of eq 28 was assessed using an F test, with degrees of freedom set at $k = 6$ for the first and $(n - k - 1 = 2)$ for the second. At a significance level of $\alpha = 0.05$, the critical $F_\alpha(6, 2)$ value is 19.33. However, the computed F value is 187.09, well above the critical threshold, indicating the model's statistical significance with a p-value below α, thus confirming the regression of eq 20 is significantly valid at the 95% confidence level.

3.2.4. Nonlinear Programming Solver Optimizing the Column Conditions. Let $y_C = a - (8.3C + 89.5/C^2)$, $y_Q = b - (6.8Q - 27.6/Q)$, and $y_H = 2.2H^{1.5} - 12.5H + m$ represent different variables under investigation in our experimental research. It has been found that the minimal value of y_H corresponds to an H value of 14.3 cm, indicating the start of our observations within the bed height range labeled $H = (25–35)$ cm. Notably, all recorded values beyond this point show an increase, establishing y_H as an increasing function in relation to H. The analysis of y_Q's derivative, being consistently negative, suggests that y_Q decreases continuously as Q increases—a trend that aligns with our empirical observations. Conversely, y_C's behavior differs; it increases with C up to a certain threshold (denoted $0 < C \ll 2.78$) and then starts to decrease

Table 2. Comparison of the Actual Effective Adsorption Capacities of the Resin with Its Predicted Values

operating conditions and the effective adsorption capacities										
C_0 (g/L)	2	6	10	4	4	4	4	4	4	
Q (mL/min)	4	4	4	3	5	6	4	4	4	
H (cm)	30	30	30	30	30	30	25	30	35	
q_{Bp}^{exp} (mg/g)	53.7	40.7	11.7	60.6	47.1	37.1	32.9	53.5	87.6	by experiments
$q_{Bp}^{pre\_MPR}$ (mg/g)	53.8	40.8	9.3	63.3	46.0	38.2	30.8	54.2	85.1	by eq 28
$q_{Bp}^{pre\_NN}$ (mg/g)	53.7	40.7	11.6	60.5	47.0	37.1	32.8	53.4	87.5	by NN model

https://doi.org/10.1021/acsomega.4c01417
ACS Omega 2024, 9, 23688−23702

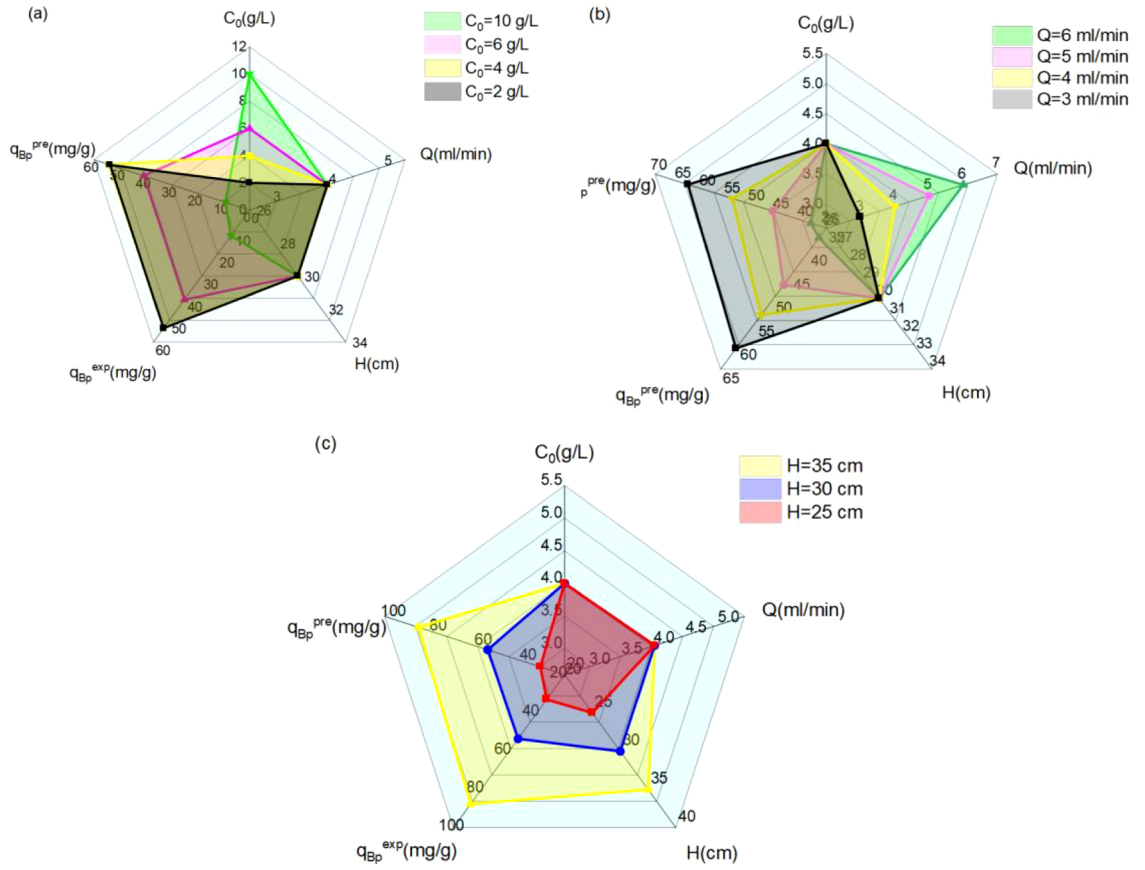

Figure 8. Comparisons of the q_{Bp}^{exp} and $q_{Bp}^{pre\_MPR}$ under (a) different initial V(V) concentrations, (b) different flow rates of feed solution, and (c) different bed heights.

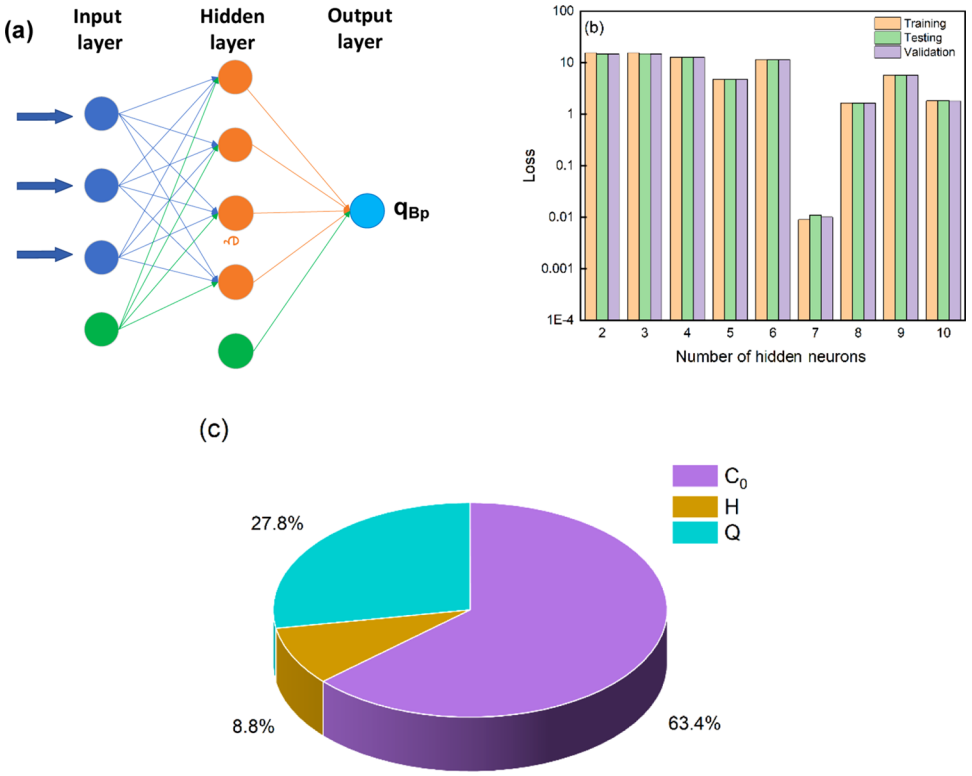

Figure 9. Analysis results of the NN model. (a) Schematic diagram of the NN model. (b) Change of loss values with the number of neurons in the hidden layer. (c) Relative importance of column operating parameters on the effective adsorption capacity of Dex-V resin.

https://doi.org/10.1021/acsomega.4c01417
ACS Omega 2024, 9, 23688−23702

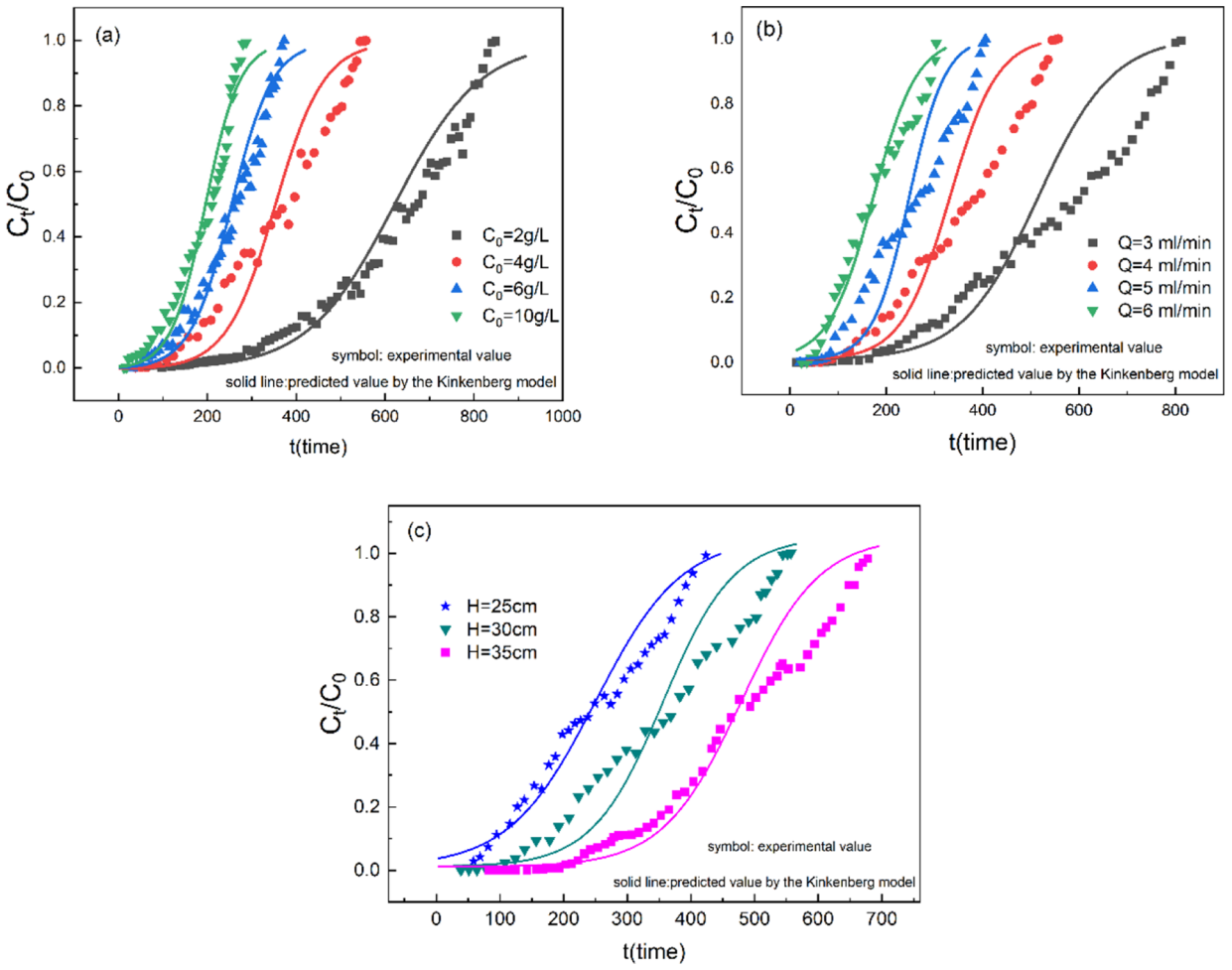

Figure 10. Theoretical breakthrough curves based on the Thomas model at different operational conditions: (a) initial V(V) concentration, (b) influent rate, and (c) bed depth.

when C exceeds this threshold (indicated as $C > 2.78$). Despite these theoretical findings, the experimental data presented in Table 2 do not reveal a clear pattern of increase followed by decrease for y_C. This inconsistency likely stems from the limited number of data points available, which hampers our ability to precisely identify the turning points in the y_C curve.

As the initial concentration of V(V) increases, a greater proportion of the resin becomes effective in targeting, thus improving its adsorption capacity within a certain time frame. However, a higher concentration of V(V) also extends the MTZ, causing the breakthrough and saturation times to occur more swiftly. This shorter breakthrough time limits the total volume of V(V) that the resin can adsorb. The interplay between these beneficial and detrimental effects indirectly explains why y_C is not a continuously decreasing function of C.

The column size specified in this study is 1.5×40 cm^2, with a design that typically leaves a 3 cm gap at the top between the column and the bed. The bed height to column diameter ratio must satisfy the $10 \ll H/D \ll 30$ requirements. Using nonlinear programming, the maximum effective adsorption capacity, q_{Bp}, was determined to be 100 mg/g under the operating conditions of C_0 = 2.8 g/L, Q = 4.4 mL/min, and H = 37 cm.

3.2.5. Analysis Results of the NN Model. A fully connected model was employed to evaluate the effective adsorption capacity of the Dex-V resin for V(V). The model consists of an input layer, hidden layers, and an output layer, as shown in Figure 9a. The input layer comprises three factors affecting the resin's effective adsorption capacity: C_0, H, and Q. The output layer represents the effective adsorption capacity of the resin, denoted as q_{Bp}. The number of neurons in the hidden layer significantly influences the model's performance. Figure 9b demonstrates the relationship between loss and the number of neurons in the hidden layer; notably, when the number of neurons is seven, the loss values for training, testing, and validation are the lowest, all below 0.012. Therefore, an NN model with seven neurons in the hidden layer can be used to predict the resin's effective adsorption capacity. The effective adsorption capacity predicted using this model, as shown in Table 2 ($q_{Bp}^{pre\_NN}$), clearly matches the experimental values (q_{Bp}^{exp}) very closely and is more accurate compared to the predictions from multiple polynomial regression ($q_{Bp}^{pre\_MPR}$).

After training, the NN model saves a weight file containing the connection weight parameters between the neurons. Following the method described by Kasiri,[42] these weight parameters can be combined to calculate the coefficients between neurons, allowing for the assessment of the importance of the three parameters, C_0, H, and Q, on the resin's effective adsorption capacity.

The relative importance of C_0, H, and Q on the resin's effective adsorption capacity, as shown in Figure 9c, is 63.39, 8.84, and 27.77%, respectively, indicating that all three are

https://doi.org/10.1021/acsomega.4c01417
ACS Omega 2024, 9, 23688−23702

Table 3. Kinetic Parameters Predicted from the Thomas Model

C_0 (g/L)	2	4	6	10	4	4	4	4	4
Q (mL/min)	4	4	4	4	3	5	6	4	4
H (cm)	30	30	30	30	30	30	30	25	35
$K_T \times 10^3$ (L/min·g)	5.16	4.57	3.61	2.28	3.40	6.34	4.90	3.99	4.13
q_0 (mg/L)	139	159	170	173	159	138	118	124	185
q^{exp} (mg/L)	148	158	168	176	161	138	115	121	190
R^2	0.88	0.85	0.84	0.70	0.88	0.81	0.71	0.88	0.88

Table 4. Kinetic Parameters Predicted from the Klinkenberg Model

C_0 g/L	Q mL/min	H cm	$k \times 10^4$ (/s)	K	$k_f \times 10^5$ (/s)	$(R_p^2/15D_p)/(R_p/3k_f)$	Sc	Sh	$D_m \times 10^9$ (m^2/s)	$D_e \times 10^{10}$ (m^2/s)	Se
2	4	30	5.738	261	7.721	**4.6**	160.161	7.610	5.580	9.190	0.052
4	4	30	5.419	100	7.721	**14.6**	160.161	7.610	5.580	2.905	0.054
6	4	30	9.222	77	7.721	**10.9**	160.161	7.610	5.580	3.900	0.053
10	4	30	6.034	62	7.721	**21.7**	160.161	7.610	5.580	1.959	0.063
4	3	30	3.303	97	7.016	**22.8**	160.161	6.915	5.580	1.692	0.048
4	5	30	5.215	87	8.317	**19.0**	160.161	8.197	5.580	2.409	0.043
4	6	30	5.943	65	8.837	**23.8**	160.161	8.711	5.580	2.041	0.034
4	4	25	4.010	84	7.721	**23.9**	160.161	7.610	5.580	1.777	0.042
4	4	35	6.693	125	7.721	**9.0**	160.161	7.610	5.580	4.701	0.034

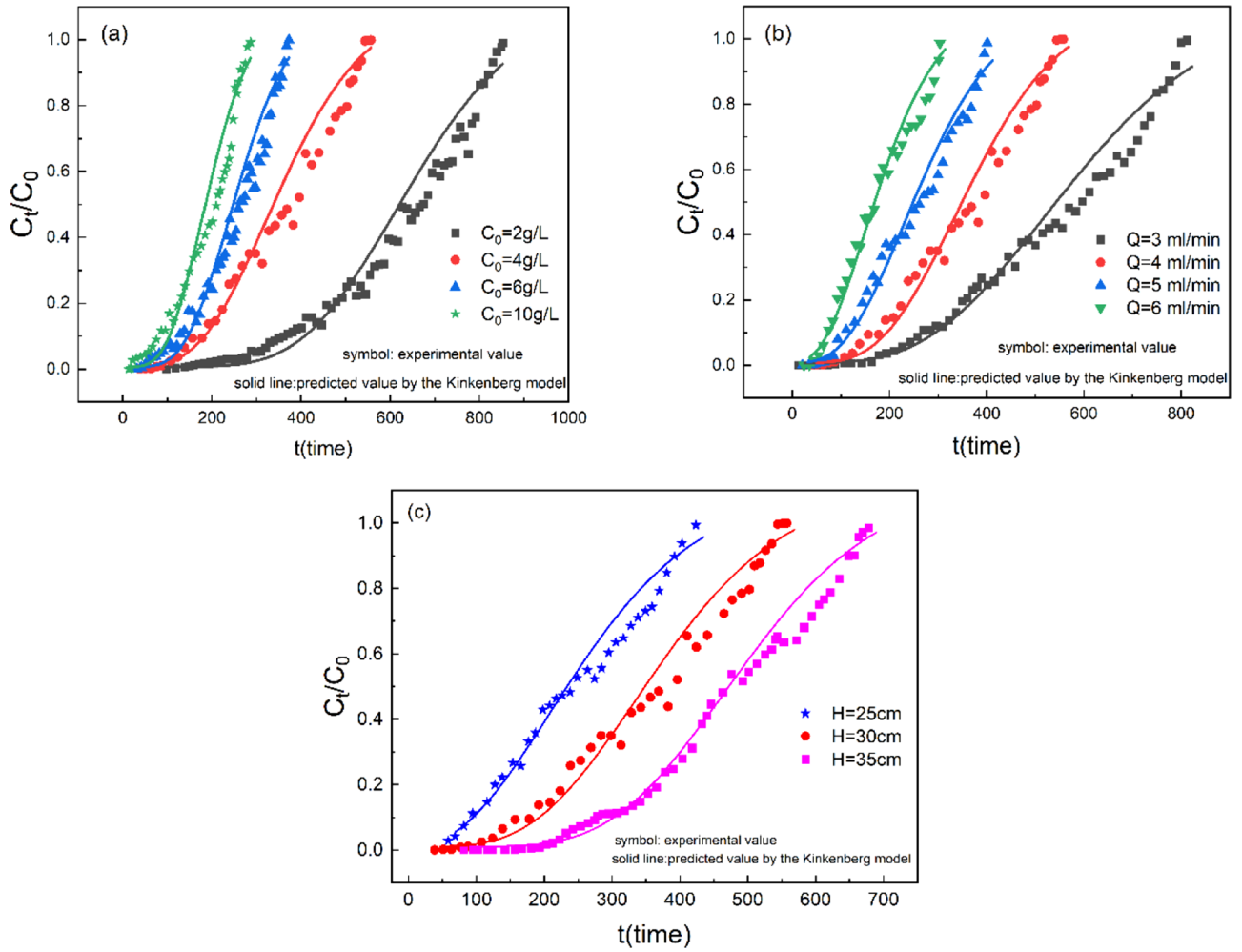

Figure 11. Predicted breakthrough curves based on the Klinkenberg model at different operational conditions: (a) initial V(V) concentration, (b) flow rate of influent, and (c) bed depth.

significant factors affecting the Dex-V resin's effective adsorption capacity. Among them, C_0 is the most significant variable, followed by Q and then H. The higher the initial concentration, the greater the driving force for solute mass

https://doi.org/10.1021/acsomega.4c01417
ACS Omega 2024, 9, 23688−23702

transfer, and the higher the frequency of contact between V(V) and the active sites, making it the most influential variable. The flow rate Q directly relates to the stagnation time of V(V) at the active sites, thus affecting the effective adsorption capacity at a given flow rate, making it the second most effective variable. The impact of column height is relatively small, possibly because Dex-V resin is a large-particle resin, with a sufficiently large number of effective adsorption sites per unit volume.

3.3. Analysis of Dynamic Properties. *3.3.1. Thomas Model.* The BTCs of the V(V) adsorption process predicted by the Thomas model are shown in Figure 10 and the correlation parameters are given in Table 3. The maximum adsorption capacity of the resin, as predicted by the model, is relatively close to the actual maximum adsorption capacity.

Data from Table 3 reveal that both metrics rise with increasing bed height, initial concentration of V(V), and as the feed rate goes up. The underlying reason is that a higher initial concentration of V(V) enhances the ions' ability to overcome liquid−solid phase mass transfer resistance, resulting in a greater number of ions exchanging per unit time. Consequently, as the initial concentration of V(V) increases, so does the observed value, and similarly, the value rises with an increase in the feed rate. Conversely, a slower feed rate decreases the height and migration speed of the MTZ, extending the average retention time of V(V) anions in the column and improving the resin's adsorption efficiency.

Therefore, the Thomas model proves to be unsuitable under slow column exchange flow rates and high initial V(V) concentrations. Our findings indicate that the Thomas model fits better when the column exchange flow rate is higher and the initial concentration of V(V) is lower. This scenario highlights the significance of intraparticle diffusion on adsorption rate, aligning with the Thomas model's assumption that intraparticle diffusion mass transfer is the limiting factor.

3.3.2. Klinkenberg Model. The analysis results of the Klinkenberg model are listed in Table 4, and the predicted BTCs are shown in Figure 11.

The Klinkenberg model predicts an S-shaped BTC, where the initial slope increases over time. This is attributed to the resin bed's inability to maintain a certain height for further downward migration of the MTZ. Toward the end of the curve, the slope decreases as adsorption approaches equilibrium, with the resin's adsorption potential weakening and the diffusion rate of V(V) slowing down.

Data from Table 4 indicate that the overall diffusion coefficient of the adsorption process increases with the initial concentration of vanadium and the feed rate of the vanadium solution but decreases as the bed height increases. However, the standard deviation values are within the range of 0 to 0.1, suggesting that the Klinkenberg method is apt for analyzing the dynamic adsorption process of Dex-V resin for V(V).

The ratio of $R_p^2/(15D_p)$ is several to dozens of times higher than that of $R_p/(3k_f)$, indicating that intraparticle diffusion has a significantly greater impact on mass transfer than film diffusion, and this impact notably increases with bed height. Consequently, it can be concluded that both intraparticle and film diffusion are limiting factors for the adsorption rate but intraparticle diffusion plays a dominant role. As the bed height decreases and the feed rate increases, the influence of intraparticle diffusion on the adsorption rate becomes more pronounced.

3.4. Dynamic Desorption of V. *3.4.1. Effect of NaOH Concentration on the Dynamic Desorption of V(V).* The dynamic desorption process is related to the flow rate of the eluate and the concentration (usage) of the eluate. Eluates of different concentrations of sodium hydroxide (2, 3, 4, 5, 6%) at the same flow rate (4 mL/min) passing through an exchange column of 30 cm bed height, the relationship between the vanadium concentration in the eluate and time is as shown in Figure 12. The higher the concentration of the eluate, the steeper the trend of the desorption curve, and the peak is higher, narrower, and sharper and tends to shift to the left as the eluate concentration increases. On the contrary, the lower the concentration of the eluent, the wider the peak of the desorption curve, and the trend is also more gentle.

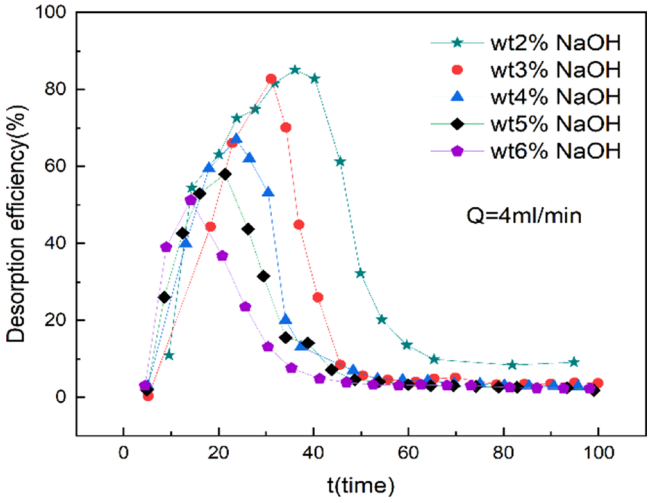

Figure 12. Dynamic elution curves for V(V) being released from load resin at different eluent concentrations.

The reason for this might be similar to the "Effect of Initial Concentration on the Dynamic Adsorption of V(V) by Dex-V Resin" mentioned above due to the increased concentration of the eluent. On one hand, the concentration of OH^- ions replacing the V(V) anionic groups increases, increasing the mass transfer driving force, facilitating the diffusion and mass transfer process of OH^- ions on the surface of Dex-V resin and within the resin particles; on the other hand, the increased concentration of OH^- ions increases their chances of full contact with the active groups of the resin.

Resins were eluted with sodium hydroxide solutions of 2, 3, 4, 5, and 6% mass concentrations, respectively. When the concentration of V(V) in the eluate flowing out from the bottom of the exchange column was detected to decrease to 0.1 g/L, the masses of sodium hydroxide consumed under the five conditions were 38.5, 40.1, 48.8, 54.2, and 52.5 g, respectively. The above data indicate that to achieve the same elution effect, the amounts of sodium hydroxide consumed under the conditions of 2 and 3% are relatively lower than those under 4, 5, and 6%, making them more economical. The difference between the amounts of sodium hydroxide used under the conditions of 2 and 3% is not significant, but the latter has a relatively higher elution speed. Therefore, considering the long-term benefits and taking into account the cost and time of the eluent, choosing a 3% NaOH solution as the eluent for this experiment is more economically reasonable.

https://doi.org/10.1021/acsomega.4c01417
ACS Omega 2024, 9, 23688−23702

3.4.2. Effect of Eluent Flow Rate on the Dynamic Desorption of V(V). Sodium hydroxide solutions with a mass concentration of 3% were passed through a V(V)-loaded exchange column with a bed height of 30 cm at flow rates of 2, 3, 4, 5, and 6 mL/min, respectively. The relationship between the vanadium concentration in the effluent and time is shown in Figure 13.

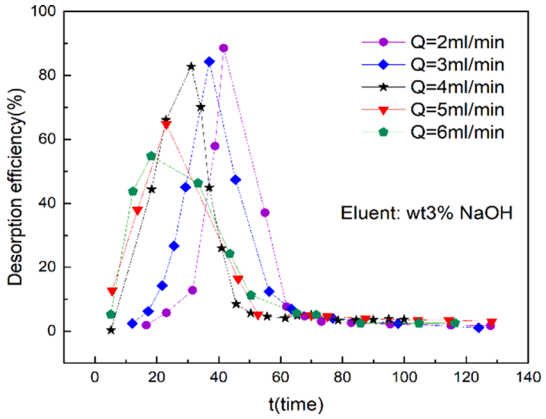

Figure 13. Dynamic elution curves for V(V) at different desorption rates.

The diagram shows that the slower the flow rate of the eluent, the more to the right the peak appears and the higher the peak becomes, with the desorption curve becoming narrower and sharper. The reason for this phenomenon is that at a slower flow rate of the eluent, fewer OH^- ions that engage in the exchange reaction with the resin are present over the same period, slowing the rate at which the saturated zone within the column moves downward. Hence, the time it takes for the peak to appear is prolonged. The slower the flow rate, the longer the average residence time of the OH^- ions in the exchange column, which enhances the effective utilization rate of the eluent. As a result, the concentration change of V(V) brought about by a unit volume of eluent is greater, making the shape of the desorption curve narrower and sharper. When the V(V) concentration in the eluent is below 0.1 g/L, the amounts of sodium hydroxide consumed at desorption rates of 2, 3, 4, 5, and 6 mL/min are 37.2, 38.8, 40.1, 52.3, and 59.1 g, respectively. Although the consumption of sodium hydroxide at a flow rate of 4 mL/min is slightly higher than at 2 mL/min, the elution rate is increased by a third. Considering both the economy and the time of the desorption process, 4 mL/min is chosen as the elution flow rate for V(V).

3.4.3. Dynamic Desorption Efficiency of the Eluent for V(V) Sodium Hydroxide. Using 3% sodium hydroxide as the eluent, the resin loaded with V(V) was eluted at a flow rate of 4 mL/min. The concentrations of vanadium and chromium in the eluent are listed in Figure 14.

The concentration of chromium in the eluent decreased hundreds of times. Before the occurrence of breakthrough behavior in the adsorption process, the solution's pH was adjusted to 8.2−8.8 to obtain precipitates of chromium hydrates. After the resin reached a state of saturated adsorption, the resin inside the exchange column was washed with a saturated carbonate solution, and finally, the resin loaded with vanadium was eluted with sodium hydroxide. The eluent was directly subjected to an ammonium salt precipitation-roasting method to extract vanadium. Experimental results indicate that the concentration of chromium in the eluent is lower than 3 mg/L, demonstrating that the Dex-V resin has a good effect on the separation of vanadium and chromium.

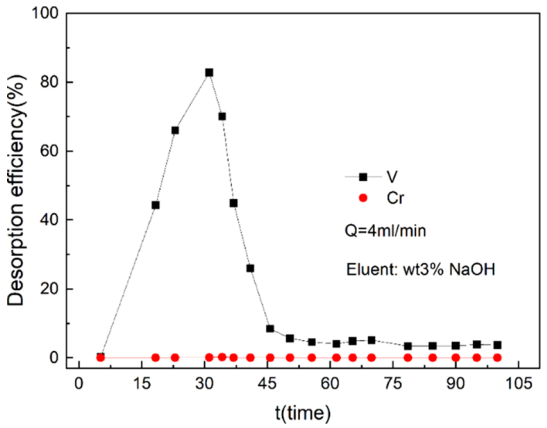

Figure 14. Dynamic desorption efficiencies of eluents on V(V).

4. CONCLUSIONS

In this study, we examined how different operating conditions of the column affect the adsorption behavior of V(V). We found that the column's most efficient use occurred at a bed height of 35 cm and a feed rate of 4 mL/min, achieving a 33% utilization rate. At these conditions, the resin's effective adsorption capacity was also at its peak, reaching 88 mg/g, alongside a relatively small MTZ height of 32 cm. As the bed height increased, both the utilization rate and the adsorption capacity improved, which can be attributed to a taller bed supporting longer MTZ formation and migration periods.

The number of MTUs declines with increases in the flow rate and solution concentration. Higher flow rates and initial concentrations lead to a lengthier MTZ and quicker migration of the saturated adsorption zone, prompting an earlier breakthrough. The resin's effective adsorption capacity within the column is denoted by $q_{Bp} = 129.0 - (8.3C + 89.5/C^2) - (6.8Q - 27.6/Q) + (2.2H^{1.5} - 12.5H)$, reaching a maximum of 100 mg/g as determined through nonlinear programming. The effective adsorption capacity predicted using the NN model is more accurate compared with the predictions from multiple polynomial regression. Analysis results of the NN model indicate that C_0 is the most significant variable, followed by Q, and then H.

Further analysis with the Thomas and Klinkenberg models confirmed that both intraparticle and liquid film diffusion play roles in adsorption rates, with intraparticle diffusion being more dominant. As the bed height decreases and the feed rate increases, the influence of intraparticle diffusion on the adsorption rate becomes more pronounced.

When using sodium hydroxide at a concentration of 3 wt % as the eluent and eluting the resin loaded with V(V) in the exchange column at a flow rate of 4 mL/min, the chromium concentration in the obtained V(V) eluate was found to be less than 3 mg/L. This reflects the method established in this study has a good vanadium−chromium separation efficiency.

This research provides both practical and theoretical insights for improving the recovery of vanadium and chromium from wastewater produced during vanadium precipitation as well as from the leachate of reduced vanadium−chromium slag.

https://doi.org/10.1021/acsomega.4c01417
ACS Omega 2024, 9, 23688−23702

AUTHOR INFORMATION

Corresponding Author

Zhuo Zuo − *The Engineering and Technical College of Chengdu University of Technology, Leshan 614000, China;* orcid.org/0000-0003-2341-177X; Email: 741153876@qq.com

Authors

Cui Li − *The Engineering and Technical College of Chengdu University of Technology, Leshan 614000, China; Southwestern Institute of Physics, Chengdu 610225, China;* orcid.org/0009-0007-0966-9367

EnDe You − *The Engineering and Technical College of Chengdu University of Technology, Leshan 614000, China*

Jia Xiang Ci − *The Engineering and Technical College of Chengdu University of Technology, Leshan 614000, China*

Qin Huang − *The Engineering and Technical College of Chengdu University of Technology, Leshan 614000, China*

Yong Sheng Zhao − *The Engineering and Technical College of Chengdu University of Technology, Leshan 614000, China*

Wen Zhong Li − *The Engineering and Technical College of Chengdu University of Technology, Leshan 614000, China*

Yu Cheng Yan − *The Engineering and Technical College of Chengdu University of Technology, Leshan 614000, China*

Complete contact information is available at: https://pubs.acs.org/10.1021/acsomega.4c01417

Notes

The authors declare no competing financial interest.

ACKNOWLEDGMENTS

Thanks to the research institute and school for providing the experimental platform. Gratitude is also extended to all the metallurgical workers involved in this work.

REFERENCES

(1) Li, H.-Y.; Li, C.; Zhang, M.; Wang, K.; Xie, B. Removal of V (V) from Aqueous Cr (VI)-bearing Solution Using Anion Exchange Resin: Equilibrium and Kinetics in Batch Studies. *Hydrometallurgy.* **2016**, *165*, 381−389.

(2) Wang, X.; Wang, M.; Fu, Z.; Meng, Y.; Gao, D.; Chen, B. Present Status and Prospects of Vanadium and Chromium Separation in Vanadium Extraction from Vanadium-chromium Slag. *Iron Steel Vanadium Titanium* **2017**, *38*, 1−5.

(3) Fang, H.-X.; Li, H.-Y.; Xie, B. Effective Chromium Extraction from Chromium-containing Vanadium Slag by Sodium Roasting and Water Leaching. *ISIJ. Int.* **2012**, *52*, 1958−1965.

(4) Wen, J.; Jiang, T.; Arken, S. Selective Leaching of Vanadium from Vanadium-chromium Slag Using Sodium Bicarbonate Solution and Subsequent in-situ Preparation of Flower-like VS2. *Hydrometallurgy.* **2020**, *198*, No. 105498.

(5) Zou, Q.; Gao, Y.; Yi, S.; Jiang, J.; Aihemaiti, A.; Li, D.-A.; Yang, M. Multi-step Column Leaching Using Low-molecular-weight Organic Acids for Remediating Vanadium-and Chromium-contaminated Soil. *Environ. Sci. Pollut. Res.* **2019**, *26*, 15406−15413.

(6) Xin, Q.; Wang, Q.; Gan, J.; Lei, Z.; Hu, E.; Wang, H.; Wang, H. Enhanced Performance in Uranium Extraction by the Synergistic Effect of Functional Groups on Chitosan-based Adsorbent. *Carbohydr. Polym.* **2023**, *300*, No. 120270.

(7) Bian, Z.; Feng, Y.; Li, H.; Wu, H. Efficient separation of vanadium, titanium, and iron from vanadium-bearing titanomagnetite by pressurized pyrolysis of ammonium chloride-acid leaching-solvent extraction process[J]. *Separation and Purification Technology* **2021**, *255*, 117169.

(8) Liu, Z.; Huang, J.; Zhang, Y.; Liu, T.; Hu, P.; Liu, H.; Luo, D. Separation and Recovery of Vanadium and Aluminum from Oxalic Acid Leachate of Shale by Solvent Extraction with Aliquat 336. *Sep. Purif. Technol.* **2020**, *249*, No. 116867.

(9) Luo, D.; Huang, J.; Zhang, Y.; Liu, H.; Hu, P. Efficient and Environment-friendly Vanadium (V) Extraction from Vanadium Shale Leachate Using Tri-n-octylmethylammonium Chloride. *Sep. Purif. Technol.* **2020**, *237*, No. 116482.

(10) Zhao, J.; Hu, Q.; Li, Y.; Liu, H. Efficient Separation of Vanadium from Chromium by a Novel Ionic Liquid-based Synergistic Extraction Strategy. *Chem. Eng. J.* **2015**, *264*, 487−496.

(11) Vinco, J.-H.; Junior, A.-B.; Duarte, H.-A.; Espinosa, D.-C. R.; Tenório, J.-A.-S. Purification of an Iron Contaminated Vanadium Solution through Ion Exchange Resins. *Miner. Eng.* **2022**, *176*, No. 107337.

(12) Livage, J. Vanadium Pentoxide Gels. *Chem. Mater.* **1991**, *3*, 578−593.

(13) Chu, K.-H. Breakthrough Curve Analysis by Simplistic Models of Fixed Bed Adsorption: In Defense of the Century-old Bohart-Adams Model. *Chem. Eng. J.* **2020**, *380*, No. 122513.

(14) Kumari, U.; Mishra, A.; Siddiqi, H.; Meikap, B.-C. Effective Defluoridation of Industrial Wastewater by Using Acid Modified Alumina in Fixed-bed Adsorption Column: Experimental and Breakthrough Curves Analysis. *J. Clean. Prod.* **2021**, *279*, No. 123645.

(15) Michaels, A.-S. Simplified Method of Interpreting Kinetic Data in Fixed-bed Ion Exchange. *Ind. Eng. Chem.* **1952**, *44*, 1922−1930.

(16) Lukchis, G.-M. Adsorption Systems. I. Design by Mass-transfer Zone Concept. *Chem. Eng.* **1973**, *80*, 111.

(17) Naja, G.; Volesky, B. Behavior of the Mass Transfer Zone in a Biosorption Column. *Environ. Sci. Technol.* **2006**, *40*, 3996−4003.

(18) Qian, W.; Song, Q.; Ding, H.; Xie, W. Computational Simulations of the Mass Transfer Zone in GS Adsorption Column Packed with Fe3+ Type Ion Exchanger. *Chemosphere.* **2019**, *215*, 507−514.

(19) Apiratikul, R. Application of Analytical Solution of Advection-dispersion-reaction Model to Predict the Breakthrough Curve and Mass Transfer Zone for the Biosorption of Heavy Metal Ion in a Fixed Bed Column. *Process Saf. Environ. Prot.* **2020**, *137*, 58−65.

(20) Tasçı, T.; Küçükyıldız, G.; Hepyalçın, S.; Cigeroglu, Z.; Şahin, S.; Vasseghian, Y. Boron removal from aqueous solutions by chitosan/functionalized-SWCNT-COOH: development of optimization study using response surface methodology and simulated annealing. *Chemosphere.* **2022**, *288*, No. 132554.

(21) Chen, C.; Chen, Z.; Shen, J.; Kang, J.; Zhao, S.; Wang, B.; Chen, Q.; Li, X. Dynamic adsorption models and artificial neural network prediction of mercury adsorption by a dendrimer-grafted polyacrylonitrile fiber in fixed-bed column. *J. Clean. Prod.* **2021**, *310*, No. 127511.

(22) Bai, S.; Li, J.; Ding, W.; Chen, S.; Ya, R. Removal of boron by a modified resin in fixed bed column: Breakthrough curve analysis using dynamic adsorption models and artificial neural network model. *Chemosphere.* **2022**, *296*, No. 134021.

(23) Plangklang, C.; Sookkumnerd, T. Modelling and Feedforward Control of Pulsed Bed Adsorption Column for Colorant Removal in Sugar Syrup. *Engineering Journal.* **2023**, *27* (1), 29−38.

(24) Stastna, M.; Grace, A. P.; Robinson, T. Exact Solutions for Flow Through Porous Media with the Klinkenberg Effect. *AIP Adv.* **2023**, *13* (1), No. 015309, DOI: 10.1063/5.0134998.

(25) Henley, E. J.; Seader, J. D.; Roper, D. K.; *Separation Process Principles*; Wiley, 2011.

(26) Woodard, S.; Berry, J.; Newman, B. Ion Exchange Resin for PFAS Removal and Pilot Test Comparison to GAC. *Remediat. J.* **2017**, *27*, 19−27.

(27) Ma, A.; Hadi, P.; Barford, J.; Hui, C.-W.; McKay, G. Modified Empty Bed Residence Time Model for Copper Removal. *Ind. Eng. Chem. Res.* **2014**, *53*, 13773−13781.

(28) Li, M.; Zhang, B.; Zou, S.; Liu, Q.; Yang, M. Highly Selective Adsorption of Vanadium (V) by Nano-hydrous Zirconium Oxide-

modified Anion Exchange Resin. *J. Hazard. Mater.* **2020**, *384*, No. 121386.
(29) Ma, A.; Abushaikha, A.; Allen, S.-J.; McKay, G. Ion Exchange Homogeneous Surface Diffusion Modelling by Binary Site Resin for the Removal of Nickel Ions from Wastewater in Fixed Beds. *Chem. Eng. J.* **2019**, *358*, 1−10.
(30) Schaefer, C.-E.; Nguyen, D.; Ho, P.; Im, J.; LeBlanc, A. Assessing Rapid Small-scale Column Tests for Treatment of Perfluoroalkyl Acids by Anion Exchange Resin. *Ind. Eng. Chem. Res.* **2019**, *58*, 9701−9706.
(31) Bai, S.; Li, J.; Ding, W.; Chen, S.; Ya, R. Removal of Boron by a Modified Resin in Fixed Bed Column: Breakthrough Curve Analysis Using Dynamic Adsorption Models and Artificial Neural Network Model. *Chemosphere.* **2022**, *296*, No. 134021.
(32) Chen, S.; Bai, S.; Ya, R.; Du, C.; Ding, W. Continuous Silicic Acid Removal in a Fixed-bed Column Using a Modified Resin: Experiment Investigation and Artificial Neural Network Modeling. *J. Water Process Eng.* **2022**, *49*, No. 102937.
(33) Allahdin, O.; Poumaye, N.; Wartel, M.; Boughriet, A. Correlation Analysis between Cationic Metal Characteristics and Ion-exchange Performance of Brick-derived Zeolites: A Comprehensive Mechanistic Explanation. *Mater. Chem. Phys.* **2022**, *276*, No. 125353.
(34) Sarwar, M.-S.; Simon, U.; Dimartino, S. Experimental Investigation and Mass Transfer Modelling of 3D Printed Monolithic Cation Exchangers. *J. Chromatogr. A* **2021**, *1646*, No. 462125.
(35) Verduzco-Navarro, I.-P.; Rios-Donato, N.; Jasso-Gastinel, C.-F.; Martinez-Gomez, A.-D.-J.; Mendizábal, E. Removal of Cu (II) by Fixed-bed Columns Using Alg-Ch and Alg-ChS Hydrogel Beads: Effect of Operating Conditions on the Mass Transfer Zone. *Polymers.* **2020**, *12*, 2345.
(36) da Costa, T.-B.; da Silva, M.-G.-C.; Vieira, M.-G.-A. Biosorption of Lanthanum Using Sericin/alginate/polyvinyl Alcohol Beads as a Natural Cation Exchanger in a Continuous Fixed-bed Column System. *Colloids Surf., A* **2021**, *627*, No. 127233.
(37) Chow, S.-J.; Croll, H.-C.; Ojeda, N.; Klamerus, J.; Capelle, R.; Oppenheimer, J.; Prasse, C. Comparative Investigation of PFAS Adsorption onto Activated Carbon and Anion Exchange Resins During Long-term Operation of a Pilot Treatment Plant. *Water Res.* **2022**, *226*, No. 119198.
(38) Al-Jaser, Z.-A.; Hamoda, M.-F. Removal of Nickel and Vanadium from Desalination Brines by Ion-exchange Resins. *Desalination Water Treat.* **2019**, *157*, 148−156.
(39) Namane, A.; Hellal, A. The Dynamic Adsorption Characteristics of Phenol by Granular Activated Carbon. *J. Hazard. Mater.* **2006**, *137*, 618−625.
(40) Virolainen, S.; Wesselborg, T.; Kaukinen, A.; Sainio, T. Removal of Iron, Aluminium, Manganese and Copper from Leach Solutions of Lithium-ion Battery Waste Using Ion Exchange. *Hydrometallurgy.* **2021**, *202*, No. 105602.
(41) Fontao, N.-C.; Hackbarth, F.-V.; Mayer, D. A.; Mazur, L.-P.; de Souza, A.-A.-U.; Vilar, V.-J.; de Souza, S.-M.-G.-U. A Step Forward on Mathematical Modeling of Barium Removal from Aqueous Solutions Using Seaweeds as Natural Cation Exchangers: Batch and Fixed-bed Systems. *Chem. Eng. J.* **2020**, *401*, No. 126019.
(42) Kasiri, M. B.; Aleboyeh, H.; Aleboyeh, A. Modeling and optimization of heterogeneous photo-Fenton process with response surface methodology and artificial neural networks. *Environmental Science & Technology.* **2008**, *42* (21), 7970−7975.

https://doi.org/10.1021/acsomega.4c01417
ACS Omega 2024, 9, 23688−23702